Solar wind driving of auroral outflow during a CME storm

Kai Zhao[1, 2], Lynn M. Kistler[2, 4], Eric J. Lund[2], Niloufar Nowrouzi[2, 3], Christopher G. Mouikis[2], and Naritoshi Kitamura[4]

[1] School of Mathematics and Statistics, Nanjing University of Information Science and Technology, Nanjing, China
[2] Space Science Center, University of New Hampshire, Durham, NH, USA
[3] Center for Space Physics, Boston University, Boston, MA, USA
[4] Institute for Space-Earth Environmental Research, Nagoya University, Nagoya, Japan

Correspondence to: Lynn M. Kistler (Lynn.Kistler@unh.edu)

Abstract. Data from the FAST spacecraft are used to study the temporal progression of the energy inputs to the dayside cusp and the nightside aurora, including Poynting flux, electron number flux and amplitude of extremely low frequency (ELF) waves, during a CME-driven storm, and the resulting H^+ and O^+ outflows. The results show that (1) On the dayside, Poynting flux, ELF waves activity and soft electron precipitation are all enhanced during the initial and main phases of the storm, and decrease during the recovery phases. On the nightside, the Poynting flux increases during the initial and main phase, but the enhancements are smaller than on the dayside. The variations in the ELF wave activity and electron precipitation are similar before and during the storm. (2) The energy inputs are strongly correlated with the solar wind - magnetosphere coupling functions, $d\Phi_{MP}/dt$ and $p^{1/2}\,d\Phi_{MP}/dt$, especially in the dayside cusp region where the energy inputs and the ion outflows are localized. (3) The O^+ and H^+ ion outflow flux, f_{O^+} and f_{H^+}, and the flux ratio f_{O^+}/f_{H^+} all increase during the storm. Both the fluxes and the flux ratio reach their peaks on the initial phase and are enhanced during the main phase. Nightside auroral H^+ and O^+ outflows have lower outflow number fluxes than that in the dayside cusp region. These observations show how the solar wind changes characteristics of CME storms and results in strong sustained ion outflow during the initial and main phases.

1. Introduction

In the Solar wind – Earth's Magnetosphere – Earth's Ionosphere (S-M-I) coupled system, energy and momentum are transferred from the solar wind to the magnetosphere and ionosphere. However, the plasma of the magnetosphere is not only contributed by the solar wind. Plasma of ionospheric origin, including O^+ ions, also populates the magnetosphere (**Shelley** et al., 1972; **Geiss** et al., 1978). The plasma from the solar wind as well as electromagnetic energy can penetrate to the ionosphere through magnetic reconnections in the dayside cusp (**Peterson** et al., 1998), heating and accelerating the ionospheric ions. The plasma of ionospheric origin gains energy and escapes from the Earth's ionosphere in both the dayside cusp region and the nightside aurora. Outflows can be either beams, which are correlated with field-aligned potential drops (**McFadden** et al., 1998; **Möbius** et al., 1998), conics, which show a significant correlation with wave activities and get energized through transverse heating (**Lund** et al., 2000), or polar wind (also called the ambipolar outflow), which consists of both low-energy ions and electrons that are moving along the field lines at high latitudes (**Ganguli**, 1996).

In recent years, statistical studies have been also carried out to investigate the dependence of the outflow on the solar wind and illumination (**Yao** et al., 2008; **Peterson** et al., 2006; **Cohen** et al., 2015), the storm time substorms (**Nosé**, et al., 2009), and the IMF control (**Hatch** et al., 2017). Using satellite observations, many studies have investigated the factors driving the escape of ions of ionospheric origin. Outflowing O^+ ions are reported to be correlated to the energy inputs, including auroral electron energy deposition (**Wilson** et al., 2001), Poynting flux (**Zheng** et al., 2005; **Strangeway** et al., 2005), soft precipitating electrons (**Strangeway** et al., 2005), broadband extreme low frequency (BBELF) waves (**Lund** et al., 1999), and Alfvén waves (**Chaston** et al., 2007; **Hatch** et al., 2016). Using the FAST observations in the dayside cusp region during a geomagnetic storm, **Strangeway** et al. (2005) evaluated the relations between the outflowing ions, measured by the ESA

instrument, and the energy inputs. They found that the Poynting flux and the electron density are the best controlling factors. Empirical models are also given in their study. Similar results were found by **Zheng** et al. (2005), using multi-instrument data from the Polar satellite. Wave-particle interactions allow ions to gain energy. At medium altitudes between 2000 km

45 and 4000 km, ions are more preferentially heated by BBELF waves than EMIC waves, which are correlated with the acceleration of He$^+$ ions (**Lund** et al., 1999). Using FAST/ESA observations, **Kitamura** et al. (2021) found that the dependence of the outflow flux on Poynting flux is not significantly affected by the solar illumination but the slope of the dependence on precipitating electron density decreases with the solar zenith angle.

50 Recent work has used a recalibrated FAST/TEAMS dataset to examine how the outflow of O$^+$ and H$^+$ vary during geomagnetic storms. **Nowrouzi** et al. (2023) used a solar cycle of FAST data to examine how the outflow varies with storm phase for different types of storms. They found that for both CME (coronal mass ejections) and SIR (streaming interaction regions) storms, the outflow peaks in the main phase, and declines, but is still significant, in the recovery phase. In addition, they found that for CME storms, there was a strong increase in outflow during the initial phase that was not observed for

55 SIR storms. **Zhao** et al. (2020) and (2022) examined the correlation between energy inputs and O$^+$ and H$^+$ outflow flux in both the dayside cusp region and the nightside auroral region for one CME-driven storm, the September 24 – 25, 1998 storm event. This is the same event examined by **Strangeway** et al. (2005). Consistent with the findings of **Strangeway** et al. (2005), the Poynting flux and the soft electron are strongly correlated with both the O$^+$ and the H$^+$ outflows in the cusp region. However, the best controlling factor for O$^+$ is the Poynting flux (r = 0.85) while the H$^+$ outflows correlate best to the

60 electron number flux (r = 0.76). In the nightside auroral region, **Zhao** et al., (2022) found that O$^+$ outflow is correlated with both Poynting flux and electron precipitation while H$^+$ outflow is only correlated with electron precipitation on the nightside.

Thus, we know that the outflow changes significantly during a storm, and we know that both precipitating electrons and electromagnetic energy input play roles in driving the outflow. The outstanding link in the chain is to understand the driving

65 factors in the solar wind that best control the energy input, leading to the storm phase-dependent ion outflow. A recent paper (**Hull** et al, 2023) examined the chain of energy flow using Cluster data in the cusp and Wind in the solar wind. They found that pressure enhancements in the solar wind and northward excursions of the IMF were associated with enhancements in Alfven wave activity and plasma, which then led to enhanced O$^+$ outflow. However, this study was for just one pass during the main phase of a storm, and did not address how the range of parameters that can occur in the solar wind will drive outflow.

70 If we understand which solar wind and IMF parameters lead to the enhanced energy input that then leads to outflow, and how these parameters change during a storm, we can use this knowledge to better predict storm development.

In this paper, we again use the September 24 – 25, 1998 CME-driven storm event to examine the changes that are observed in the solar wind and IMF as the storm progresses, and how those are related to the changes in the energy input and the

75 outflow in the cusp and nightside auroral regions. In particular, we will address: (1) How do the energy input and the outflow flux change with time during the storm? (2) Which solar wind drivers are responsible for the enhanced energy input? In section **2.1**, the September 24 – 25, 1998 geomagnetic storm will be reviewed in brief. In section **2.2**, the FAST/TEAMS measurement is introduced, and the data sets of this study are shown. In section **2.3**, we introduce how we calculate the parameters. Results will be given in section **3**, where the proposed questions will be discussed in sections **3.1 – 3.4**.

80 Discussion and conclusions are given in section **4**.

2. Methodology

2.1 Overview of the geomagnetic storm

An interplanetary shock from a large CME arrived at the Earth's magnetopause with a space speed of 769 km/s at 23:45:00 UT on September 24, 1998 (**Russell** et al., 2000). It was observed at 1998-09-25/00:00:00 by the FAST satellite when it

85   entered the dayside cusp region, 16 mins later. During the storm, the Earth's magnetopause was moved inward and the dayside magnetospheric boundaries are pushed tailward. Significant energy was injected into the ionosphere in both the dayside cusp region and the nightside auroral oval zone, producing remarkable outflows.

Figure **1(A)** panels (**a**)-(**c**) show the interplanetary magnetic field (IMF) and the solar wind dynamic pressure (P_{dyn})
90   propagated to the Earth's magnetopause. IMF first turns northward and starts to show strong perturbations at around 1998-09-24/23:45:00. The IMF Bz component alternates between northward and southward, fluctuating between 20 nT and –20 nT. Meanwhile, the Dst index (panel (**e**)) sharply increases by 45 nT after the pulse of the shock, indicating the SSC. The IMF Bz component (panel (**b**)) reaches its first minimum of –20 nT at 1998-09-25/00:21:30, when the solar wind dynamic pressure approaches its first peak value of 14 nPa. The Kp index is 7^{+} at the sudden storm commencement (SSC), as shown
95   in panel (**g**). Panel (**h**) shows the quantity $\sin(\theta_c/2)$, an indicator of the southward orientation of the IMF, with 1 for a purely southward field and 0 for a northward field. Panels (**i**) and (**j**) show two solar wind-magnetosphere coupling functions

$d\Phi_{\mathrm{MP}}/dt$ and $p^{1/2}\,d\Phi_{\mathrm{MP}}/dt$, from **Newell** et al. (2007). The first, $d\Phi_{\mathrm{MP}}/dt = v^{\frac{4}{3}}B_T^{\frac{2}{3}}\sin^{8/3}(\frac{\theta_c}{2})$, combines the information from the rate IMF field lines approaching the magnetopause (proportional to the solar wind speed v), the percentage of the field lines merging (proportional to $\sin^{8/3}(\frac{\theta_c}{2})$, where θ_c is the IMF clock angle), and the length of the merging line

100   (proportional to $\left(\frac{B_{MP}}{B_T}\right)^{1/3}$, where B_T is the IMF magnitude and B_{MP} is the field magnitude at the magnetopause), to give an approximation to the rate magnetic flux is opened at the magnetopause. This function has been found to correlate well with many indicators of geomagnetic activity. The second function, which is scaled by the dynamic pressure, was found to have a better correlation with Dst (**Newell** et al., 2007). As shown in the plot, multiple parameters change during the storm. Bz drops significantly during the storm main phase, while the dynamic pressure increases significantly. In addition, the intensity
105   of both coupling functions increase during the initial phase of the storm, remain enhanced during the main phase, and decline during the recovery phase. In section **3.4**, we will calculate the correlations between the different drivers and the energy inputs to discuss the factors driving the energy inputs to the ionosphere, which accelerate ions to outflow.
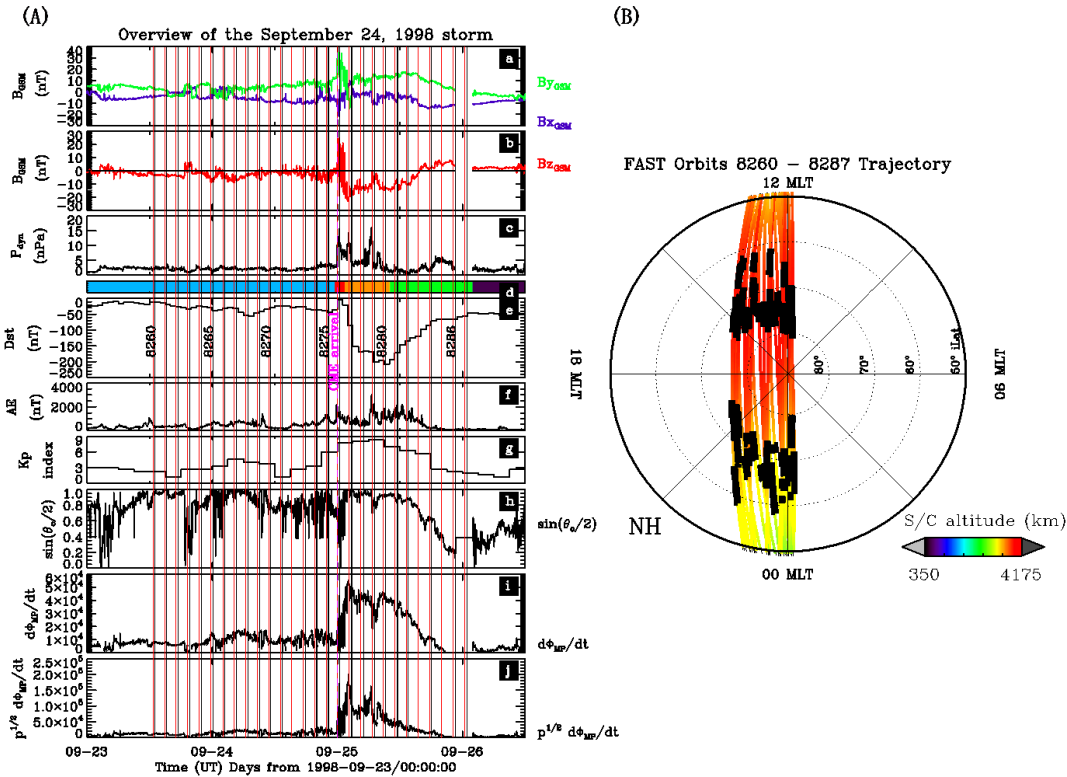
Figure 1. Left-hand plot (**A**): overview of the storm. From top-down, the plot shows (**a**) the interplanetary magnetic field Bx and By, (**b**) Bz, (**c**) the solar wind dynamic pressure, (**d**) the color code of the storm phase (blue for pre-storm times, dark red for the initial phase, orange for the main phase, and green for the recovery phase), (**e**) the Dst index, with some orbit numbers labelled at the vertical lines which indicate the start times of the dayside outflows (in red) and the nightside outflows (in black), (**f**) the AE index, and (**g**) the Kp index, (**h**) $\sin\left(\frac{\theta_c}{2}\right)$, where θ_c is the IMF clock angle, (**i**) the rate magnetic flux is opened at the magnetopause, $d\Phi_{MP}/dt$, and (**j**) $p^{1/2}d\Phi_{MP}/dt$, where p is the solar wind dynamic pressure (**Newell** et al., 2007). The magenta vertical line indicates the time of the coronal mass ejection (CME) arrival. Right-hand plot (**B**): trajectories of the 28 FAST orbits. The coordinate system is magnetic local time by magnetic invariant latitude. The Sun is in the upward direction. The bolded segments represent the time intervals when outflows are observed in either the nightside auroral oval zone or the dayside cusp region, as **Strangeway** et al. (2005) did but they used 33 orbits and considered data acquired only on the dayside. The color code indicates the spacecraft altitude above the Earth's surface.

The FAST spacecraft was traveling through the dayside cusp region over the polar cap to the nightside auroral oval zone, observing a large amount of H⁺, He⁺, and O⁺ outflows. The arrival time of the coronal mass ejection, during orbit 8276, is marked by the magenta vertical line in Fig. **1**(**A**) (see **Strangeway** et al., 2005 and **Zhao** et al., 2020 for the summary plot of this orbit).

2.2 Instrumentations and data sets

Fast Auroral Snapshot Explorer (FAST) travels through the auroral oval four times each orbit (133 mins orbital period) at altitudes from 350 km to 4175 km, due to its orbit configuration with a high inclination angle (83 degrees). It was designed to study the particle transportations and accelerations in the polar ionosphere, providing measurements of the electric and

magnetic fields, plasma waves, energetic particles including electrons and ions, ion composition, and the density and
temperature of plasma with a high temporal (microseconds) and spatial resolution (**Pfaff** et al., 2001; **Carlson** et al., 2001;
Ergun et al., 2001; **Elphic** et al., 2001; **Klumpar** et al., 2001), allowing us to study the process of the outflows, electric
currents, and plasma waves in the magnetosphere-ionosphere coupling system. There are four scientific instruments and an
instrument data processing unit (**Harvey** et al., 2001; **Pfaff** et al., 2001).

This study uses the data from all the instruments. The Electrostatic Analyzer (ESA) measures the electron (eESA) and ion
(iESA) distribution function over a 180 degree of field of view (FOV) in 48 energy channels and 32 pitch-angle bins every
78 ms (**Carlson** et al., 2001). The measured energy ranges from 4 eV to 32 keV for electrons and 4 eV to 25 keV for ions.
The Electric Field Sensors (**Ergun** et al., 2001) and the Magnetic Field Experiment sensors (**Elphic** et al., 2001) measure
electric field data, plasma density, and temperature, and magnetic field data. The electric field covers frequencies from DC
(0 Hz) to ~2 MHz. The AC magnetic field data spans frequencies from 10 Hz to 500 kHz. The TEAMS instrument measures
the full 3D distribution function of the major ion species (including H^+, He^+, O^+) with an instantaneous 360×8 field of view
with energies between 1 eV/charge and 12 keV/charge. The time resolution depends on the mode of the instrument. At the
fast-sampling mode, the data is transmitted to the ground every 2.5 seconds (a half spin period), while the data is transmitted
every 10 or 20 seconds (2 or 4 spins) for H^+ and O^+ in slow modes (**Klumpar** et al., 2001).

Recently, the TEAMS instrument has been recalibrated by similar methods to those used for the similar Cluster/CODIF
instruments (**Kistler** et al., 2013). The calibration methods are described in **Zhao** et al. (2022) and the appendix section of
Nowrouzi et al. (2022). This study uses the level 2 pitch-angle energy product for the TEAMS analysis. The level 2 datasets
are available at the NASA Space Science Data Center (NSSDC).

FAST observations are selected during the period from 12:00:00 UT on September 23, 1998 to 01:00:00 UT on September
26, 1998. There are 28 orbits during the period, with 16 orbits before the storm, 1 orbit during the initial phase, 4 orbits
during the main phase, and 7 orbits during the recovery phase. The start times of the dayside outflows and the nightside
outflows are marked by the red and black vertical lines, respectively, in Fig. **1(A)**. The trajectories during this time are near
the noon-midnight meridian plane, covering the cusp region and the nightside aurora. Outflows, including both H^+ and O^+,
are observed by FAST in those regions, allowing us to investigate the change in the outflows with time from the dayside cusp
and nightside aurora zone and make a comparison between the two source regions. Figure **1(B)** shows the trajectories
of the orbits in this study. The outflow time intervals are shown in bold lines. The method used to identify the outflow time
intervals is described in **Zhao** et al. (2022). Some orbits show multiple bold intervals because the nightside outflow is not
continuous and can occur at multiple latitudinal locations. The source region of the outflows has good coverage in magnetic
local time (MLT) from 21:00 to 01:00, and in ILAT from 60 to 80 degrees. There are a total of 865 (1114) spin-averaged
measurements (the spin period is 5 seconds at the fast mode) for O^+ and H^+ collected by the TEAMS instrument in the
nightside (dayside) source region. All observations are collected above 2500 km altitude, and more than 92% are collected
between 3000 km and 4000 km. The average altitude is ~3400 km (~4100 km) for the observations on the nightside (dayside).
All fluxes, including the H^+ and O^+ outflow number flux, the Poynting flux, the electron energy flux, and the electron number
flux, are mapped to 100 km.

The FAST field instruments can measure the electric field components E_x, E_z and the magnetic field B = (B_x, B_y, B_z). The
E_x component is along the spacecraft velocity in the northern hemisphere (in the southern hemisphere, it is anti-parallel to
the spacecraft velocity) and E_z is near the magnetic field direction at high latitudes. The three components of the magnetic
field are determined in both the spacecraft spin plane coordinates (B_{sc}) and the geocentric equatorial inertial coordinates
(B_{gei}). The difference in the magnetic field, δB, is calculated in field-aligned spacecraft coordinates, with δB_x along the
spacecraft velocity vector, along track, δB_y in the direction of B cross spacecraft velocity vector, across track, and δB_z along
the model magnetic field B. This study focuses on the downward Poynting flux, $S = E_x \cdot \delta B_y / \mu_0$, where μ_0 is the

175   permeability of vacuum.

2.3 Calculations of the energy-input parameters and the outflow flux

The parameters analyzed in this study include (1) the number flux of the individual ion species, H^+ and O^+, recorded as f_{H+} and f_{O^+}, respectively, (2) the amplitude of the extremely low frequency (ELF) waves, recorded as A_{elf}, (3) the quasi-static Poynting flux, S_{dc}, (4) the Alfvénic Poynting flux, S_{ac}, and (5) the electron number flux, f_{en}. We also use P_{dyn}, B_Z, and the

180   two **Newell** et al. (2007) coupling functions to analyze the correlation of between the energy input and the solar wind parameters.

The outflow flux and the energy input parameters are determined from the FAST data by the same method as described in **Zhao** et al. (2020, 2022). The outflow number flux is calculated by integrating the differential energy flux aligned to the

185   field line over energy and over pitch angle. The energy is integrated from 1 eV to a dynamic energy, E_{dyn}, which separates the outflowing ions from the isotropic ions of plasma sheet origin (see **Hatch et al.**, 2020, for details of the method). The pitch angle ranges from 0 to 180 degrees so that it gives the net flux. The ELF waves cover the frequencies from 32 Hz to 16 kHz, a combination of the very low frequency (VLF) and the ELF bands (**Ergun** et al., 2001). The amplitude of the waves is calculated by integrating the electric field power density over the frequencies covering the band from 32 Hz to 16 kHz

190   collected from 118 frequency channels. Thus, the band covers high-frequency Alfvén waves, oxygen and hydrogen cyclotron waves, low-frequency whistler mode waves, and BBELF waves. The eESA data is used to determine the electron number flux. The electron fluxes are integrated over energies above 50 eV to exclude the photoelectrons. The despun magnetic field (**Strangeway** et al., 2005) is sorted into two frequency bands, 0.125 – 0.5 Hz, corresponding to the fluctuations of Alfvénic waves, and < 0.125 Hz, corresponding to the quasi-static fluctuations. Thus, the DC Poynting flux, S_{dc}, is associated with

195   the fluctuations below 0.125 Hz, while the Alfvenic Poynting flux covers the frequencies of 0.125 – 0.5 Hz.

We first determine the time intervals of the outflows by the method described in **Zhao** et al. (2022). Once the time intervals are determined, averages or maxima are calculated for all the quantities over the time interval. In this study, averages are obtained for the outflow fluxes, the electron number flux, and the amplitude of ELF waves, while maxima are computed for

200   the Poynting fluxes. The beginning and ending times of the outflowing intervals are the same as **Zhao** et al., 2022. The day side picks up the cusp and surrounding region broadly, while the night side picks up only a small part of the auroral zone where significant outflows are observed. In the 28 FAST orbits (numbered from 8260 to 8287), there are 5 orbits on the nightside (8272, 8283; 8270, 8271, 8278) and 5 orbits on the dayside (8260, **8270**, 8271, 8272, 8280) with no TEAMS observations (the instruments were off during the time period) or with significant TEAMS data gaps during the outflow time

205   period. These time periods are not used for the TEAMS data. There are a few orbits on the nightside with multiple outflow regions, and we use the most poleward region, which has the largest outflow. In addition, the nightside H^+ number flux is too low in orbit 8285, so that time period is deleted from our study. Thus, we have 23 outflow time periods on the dayside and 22 outflow time periods on the **nightside**. The iESA data and the energy input data are available for all 28 orbits. With these samples, the questions proposed in the introduction section will be discussed in the following sections.

210   **3. Observations**

3.1 Sample orbits during the storm

Figure **2** shows the data quantities of this study for three orbits: orbit 8275 (left panel (**A**)), before the SSC of the storm, orbit 8277 (middle panel (**B**)), two hours after the SSC, and orbit 8279 (right panel (**C**)), towards the end of the main phase, indicating the progression during the storm. FAST was moving through the dayside cusp region over the polar cap and over

215   the nightside auroral oval zone during each orbit, as shown at the far right in the plot. For each orbit, the panels, from top to bottom show (**a**) electron spectrograms from the eESA instrument, (**b**) omnidirectional ion spectrum from the iESA

instrument, (**c**)-(**d**) H⁺ and O⁺ omnidirectional energy spectra from the TEAMS instrument, (**e**)-(**f**) pitch angle distributions of H⁺ and O⁺ integrating from 1-500 eV, (**h**)-(**k**), the DC Poynting flux, the Alfvenic Poynting flux, the electron number flux, and the amplitude of the ELF waves. Panel (**l**) shows the ion outflow flux for the three species H⁺, O⁺, He⁺, as well as the

220 all-ion outflow flux from the iESA instrument. We note that there are significant differences between the iESA instrument and the TEAMS instrument. Their minimum energy is slightly different, the iESA measures a 2D distribution while TEAMS measures the full 3D distribution, the iESA is more susceptible to penetrating electron background, and TEAMS requires a large dead time correction during high fluxes, which leads to a larger uncertainty. Thus, we do not expect the two measurements to be identical, but we certainly expect them to show the same trends.
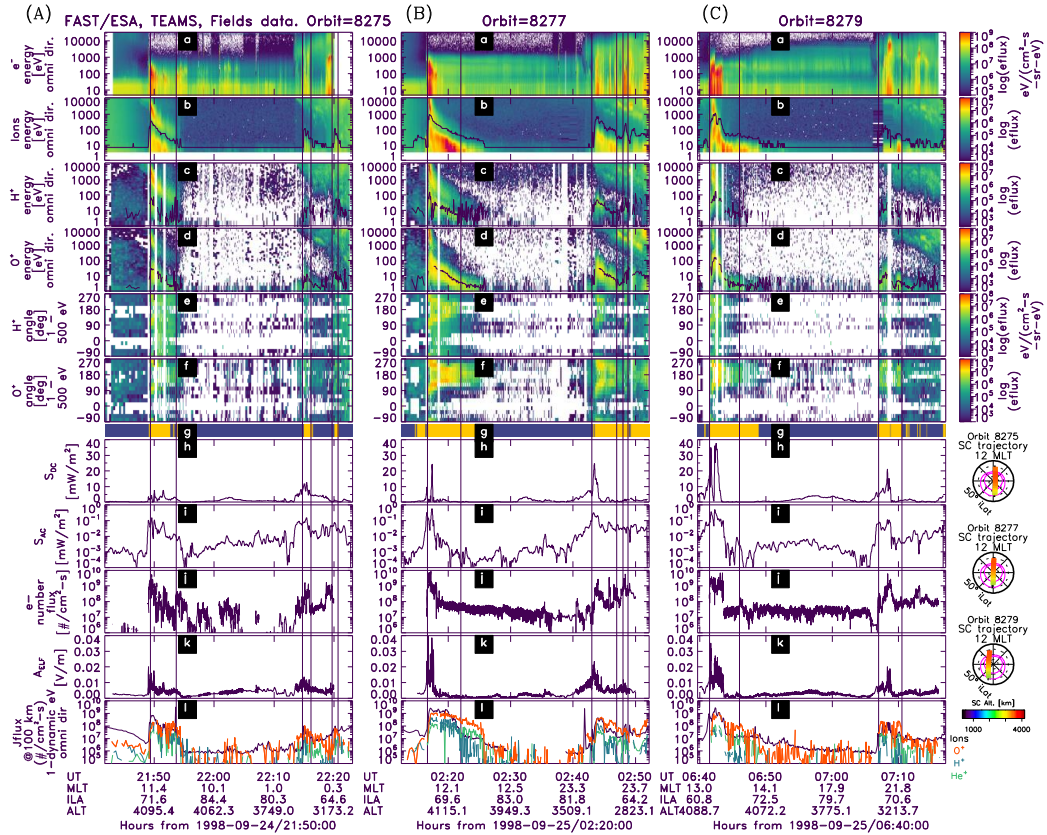
225

Figure 2. The FAST observations in orbit 8275, left panel (**A**), before the storm sudden commencement (SSC), orbit 8277, middle panel (**B**), during the main phase of the storm, and orbit 8279, right panel (**C**), near the end of the main phase. From top down, this plot shows (**a**) the electron energy-time spectrogram, (**b**) the ions energy-time spectrogram, with the cutoff energy (black line) superimposed determined by the ESA instrument, (**c**) the TEAMS H⁺ energy-time spectrogram with the

230 characteristic energy (black line) superimposed, (**d**) the TEAMS O⁺ energy-time spectrogram with the characteristic energy (black line) superimposed, (**e**) the TEAMS H⁺ pitch angle spectrogram for energies between 1 eV and 500 eV, (**f**) the TEAMS O⁺ pitch angle spectrogram for energies between 1 eV and 500 eV, (**g**) the outflow bar, showing the outflow time interval with yellow, (**h**) the quasi-static Poynting flux related to <0.125 Hz fluctuations, (**i**) the Alfvenic Poynting flux covering frequencies of 0.125 – 0.5 Hz, (**j**) the 50 eV – 35 keV electron number flux, (**k**) the amplitude of ELF waves covering

235 frequencies of 32 Hz – 16 kHz, (**l**) the field-aligned number flux f_{O^+} for O⁺ (red), f_{H^+} for H⁺ (blue), and f_{He^+} for He⁺ (green). The outflow flux measured by iESA is overplotted (black line). Data will be averaged over the outflow time in the dayside cusp (the first couple of the vertical lines), the poleward segment of the nightside aurora (the second couple of the vertical lines), and the equatorward of the nightside aurora (the third couple of the vertical lines). The trajectories of the three

240   orbits are shown in the right-side small dial plots, with the magenta line indicating the empirical location of the auroral oval zone.

The first orbit illustrates the energy input and outflow during a relatively quiet time. The plot shows the passage through cusp from ~21:49−21:53 and the passage over the nightside aurora from ~21:14−21:21. The cusp has two ion populations, a higher energy latitude-dispersed population that is predominantly H^+ and a lower energy population that is predominantly

245   O^+. The high-energy population is the magnetosheath population entering through reconnection (**Peterson** et al., 1998). The latitude dispersion is due to a time-of-flight effect due to the tailward convection of the reconnected field line, with higher energy ions entering earlier than lower energy ions (**Connor** et al., 2015). The pitch angle distributions show that the low energy population consists of upflowing conics. The nightside aurora also shows two ion populations. In this case, the higher energy population is the plasma sheet precipitating or mirroring at low altitudes. The low energy population is

250   dominantly O^+ and has a conic distribution. Panels (**h**)-(**k**) show that in both the cusp and nightside auroral regions, the DC and AC Poynting flux, the precipitating number flux, and the EFL amplitude are enhanced. The resulting outflow from the upflowing conic distributions is seen in panel (**l**). This shows that even prior to a storm, during relatively quiet time, there is energy input and outflow in the cusp and auroral regions. The next two orbits show the changes during the storm. In orbit 8277, after the SSC, the DC and AC Poynting flux and precipitating electrons are all enhanced, particularly close to the low

255   latitude boundary. This drives much stronger outflow, evident both in the energy and pitch angle spectra, and in the number flux. The outflow number flux increases by an order of magnitude from 10^8 ions/cm^2-s to 10^9 ions/cm^2-s in the cusp, as shown by panel (**l**). The nightside auroral region also has increased energy input, in particular close to the polar cap boundary, which also drives enhanced outflow. In the 3rd orbit, the cusp S_{dc} exceeds 35 mW/m^2, while f_{en} reaches $5×10^9$ ions/cm^2-s, driving strong localized outflow. Although the precipitating electrons are still intense on the nightside, the Poynting flux and

260   the wave activity have decreased. As a result, the outflows become less intense.

3.2 Energy and pitch angle distributions of H^+ and O^+ outflows

The progression of the O^+ and H^+ outflows during the storm can also be seen in the energy–pitch angle distributions. The TEAMS data is sorted into an array with 48 energy channels and 16 pitch angle directions. The data are averaged over the outflowing time interval by the method described above to get the energy – pitch angle distributions. The pitch angle goes

265   from 0 to 360 degrees, considering the 360 degrees field of view (FOV) of the TEAMS instrument. The energy of the ions moving in the direction of the pitch angle 0 represents the parallel velocity, $V_{\parallel}$ (units, eV), while the energy of the ions moving in the direction of either pitch angle 90 or 270 degrees represents the perpendicular energy, $V_{\perp}$ (units, eV). Based on the distribution, we can compare the characteristics and the intensity of the outflows from different ion species and different locations.

270

Figure **3** shows the energy–pitch angle distribution of O^+ and H^+ outflows from the nightside aurora and the dayside cusp region, respectively. The time gap between two distinct orbits is about 2 hours. Orbit 8278 was an orbit with a large data gap during the outflow time on the nightside for TEAMS. As was observed in the energy spectra in Fig. **2**, two populations are evident in each panel. The first, the ion outflow, is seen at the center of each panel, the low energies, with a pitch angle

275   distribution symmetric about 180 degrees, and peaks located between 180 and 90 (or 270) degrees. These are the classic conic distributions, which result from wave acceleration at or below the observation location. The second population is at high energies, and relatively isotropic except for the low flux in angles close to 180 degrees. On the nightside, this is the precipitating plasma sheet distribution, while on the dayside it is the entering magnetosheath population.

280   The top row shows the O^+ distributions on the nightside. Before the storm, in orbits 8274 and 8275, as indicated by the blue mode bar, the outflow flux is comparatively low. The conic population becomes most intense just after the storm onset, orbits 8276 and 8277. Later in the main phase, the outflows become less intense and less energetic. The second row shows H^+ on the nightside. The low-energy H^+ ions also show the conic distributions. For the H^+, the precipitating plasma sheet

distribution is more continually present than for the O⁺. While there are clearly conics in orbits 8276 and 8277 after the

285   storm commencement, they are not significantly more intense than some of the pre-storm orbits, such as the orbits 8265 and

8267 (not shown in Fig. **3**) when the outflow flux is comparable to that of orbits 8276 and 8277.
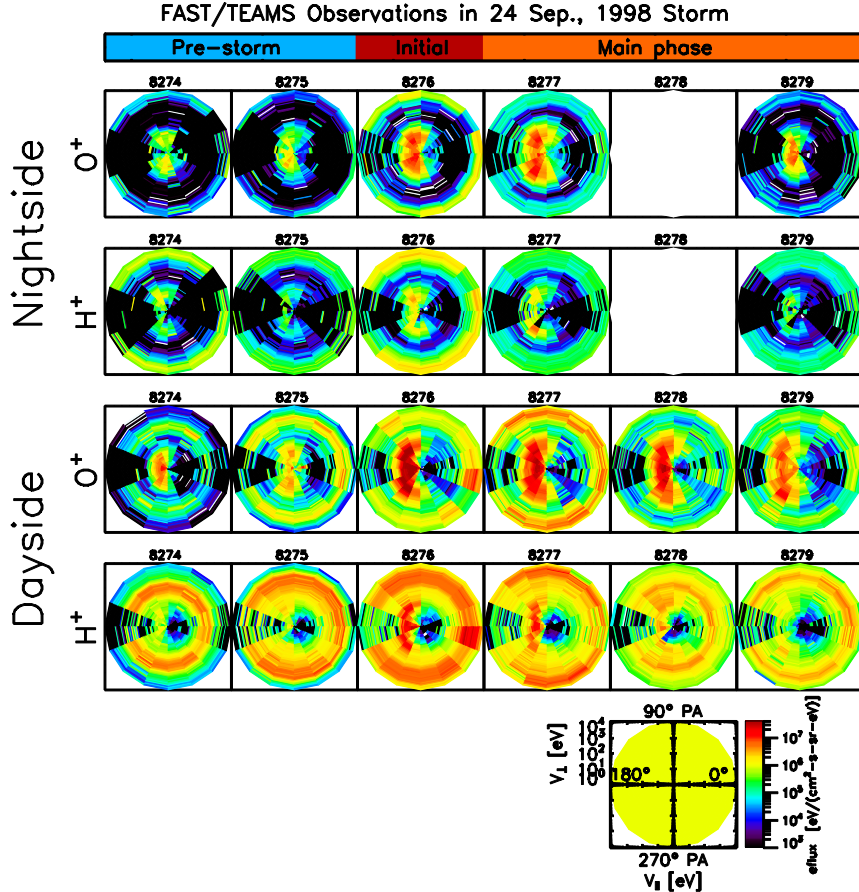
Figure 3. Energy – pitch angle plots of the outflowing number flux for the nightside aurora O⁺ (top row), the nightside aurora H⁺ (second row), the dayside cusp O⁺ (third row) and the dayside cusp H⁺ (fourth row), averaged over each outflowing time

290   interval. It shows six consecutive orbits with two orbits (8274 and 8275) before the storm, one orbit (8276) on the initial phase and three orbits (8277-8279) on the main phase. Only the poleward segment of the nightside outflows is shown in this plot. Energy from 0.9 eV to 12 keV is divided into 48 bins. Pitch angle, ranging from 0 to 360 degrees, is divided into 16 pitch angle directions. The field line direction points to the right and the anti-field line direction points to the left, as shown by the right-bottom plot. The orbit number is labeled on the top of each panel. SSC occurs in orbit 8276. Panels for the

295   nightside outflows in orbit 8278 are blank due to the data gap.

The third and fourth rows show the O⁺ and H⁺ distributions in the cusp. Overall, the cusp outflows are more intense than the nightside outflows. O⁺ shows a similar dependence on storm phases to the nightside. The flux is suddenly enhanced to its peak at the SSC to the level of 10^9 ions/cm²-s and is intense during the main phase. The O⁺ flux is higher on the dayside than

300   the nightside during the storm. The H⁺ outflow characteristics are similar, but less intense than O⁺. The precipitating population, from the magnetosheath, is much stronger for H⁺ than for O⁺.

3.3 Responses of the outflow to the energy input

The correspondence of the outflow flux with the energy input over the time history of the storm is shown in Fig. **4**, with cusp on the left and nightside on the right. Panels (**c**) and (**j**) show both the O⁺ flux and the all-ion flux. The fluxes track very

305   well. As was seen in Fig. **3**, the cusp O⁺ flux (panel (**c**)) shows a clear strong increase in the initial phase, stays enhanced during the main phase, then returns to the level of the pre-storm times. The averaged intensity of O⁺ outflow in the nightside aurora (panel (**j**)) is generally weaker than the dayside cusp region (panel (**c**)). It also increases during the initial and early main phase, and then decreases. There is also a pre-storm increase in O⁺ in orbit 8265 and 8267, so the trend is less clear. The H⁺ ion outflow flux is shown in Fig. **4** (panels (**d**) and (**k**)). The cusp H⁺ has a clear peak during the initial phase and

310   then decreases. As was clear in Fig. **3**, the nightside H⁺ outflows are less affected by the conditions during storm times than the O⁺ outflows, with only a small increase, no larger than observed during some pre-storm periods.
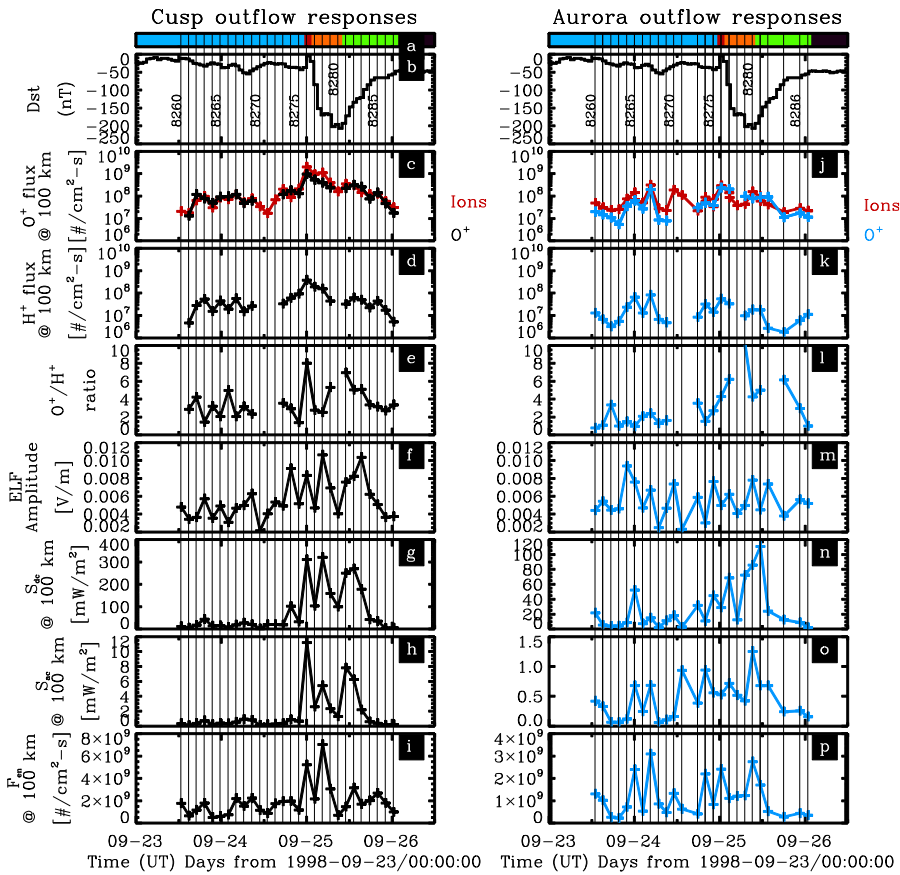
Figure 4. The evolution of the dayside cusp (left plot) and the nightside aurora (right plot) O⁺ and H⁺ outflows and the energy inputs during the storm. It shows (**a**) the storm phases (the color is the same as Fig. **1**), (**b**) the Dst index, with some

315   orbit numbers labeled, the averaged O⁺ outflowing number flux and the iESA outflow number flux, mapped to 100 km, over the dayside cusp region (**c**) and the nightside auroral oval zone (**j**), the averaged H⁺ outflowing number flux (**d** and **k**), the averaged O⁺/H⁺ flux ratio (**e** and **j**), and the averaged energy inputs, including (**f** and **m**) A_{elf}, (**g** and **n**) S_{dc}, (**h** and **o**) S_{ac}, and (**i** and **p**) f_{en} over each dayside outflow segment and each poleward nightside outflow segment. The vertical reference line represents the start time of each outflow segment. There are 27 segments on the dayside since the orbit 8280 is excluded

320   due to large fraction of missing data. There are 25 segments on the nightside as explained in section **2**.

The cusp energy input shows a very coherent storm-phase picture, with the ELF amplitude, S_{ac} and S_{dc} and f_{en} all increasing at storm onset. S_{ac}, reaches its maximum at the SSC while S_{dc} reaches its first peak value at the SSC, and both remain enhanced into the recovery phase. The wave activities and the precipitating electrons are most intense during the main phase.

325   The nightside response is much less coherent. The nightside Poynting flux, S_{dc}, is enhanced during the storm time while the ELF wave activity, S_{ac}, and the electrons are variable throughout the magnetically quiet and active times, with no clear enhancement during the storm.

The O$^+$/H$^+$ flux ratio, panels (**e**) and (l), show a clear dependence on the storm phase. On the dayside, the ratio increases

330   from a mean of 2.8 before the storm to 8.0 during the initial phase and ~4.0 during the main and recovery phases. On the nightside, it starts lower, at 1.9 before the storm, increasing to 4.3 during the initial phase, 5.8 in the main phase, and 3.8 in the recovery phase. Thus, the storm increases the average O$^+$/H$^+$ flux ratio by a factor of 1.5 on the dayside and 2.5 on the nightside (ratio of storm-time average to quiet-time average). The O$^+$/H$^+$ changes more on the nightside than on the dayside during the storm mainly because of the small change in the H$^+$ flux on the nightside, and because the O$^+$/H$^+$ ratio is higher

335   before the storm on the dayside.

3.4 Solar wind controlling the energy input

To find the driving factors of the energy inputs, we test the correlation between the well-known drivers of magnetospheric response, IMF Bz and solar wind dynamic pressure. In addition we test the solar wind-magnetosphere coupling function (**Newell** et al., 2007), $d\Phi_{\mathrm{MP}}/dt = v^{\frac{4}{3}} B_T^{\frac{2}{3}} \sin^{8/3}(\frac{\theta_c}{2})$, which, as described in section **2.1**, estimates the rate of magnetic

340   reconnection at the magnetopause. We use this function because **Newell** et al. (2007) found it a better parameter for representing the interaction between the solar wind and the magnetosphere than other coupling functions, including Bz, the solar wind dynamic pressure p, the half-wave rectifier vBs, and $\varepsilon = vB_T^2 \sin^4(\frac{\theta_c}{2})$. In addition, because we are examining the changes in the outflow during a storm, we also test the modified coupling function, $p^{1/2} d\Phi_{\mathrm{MP}}/dt$, which was found to have the best correlation with Dst.

345

Figure **5** shows the dependence of the three energy inputs on the drivers. Intensities of the drivers and the energy inputs are averaged over the time periods of outflows on the dayside and the nightside, respectively.
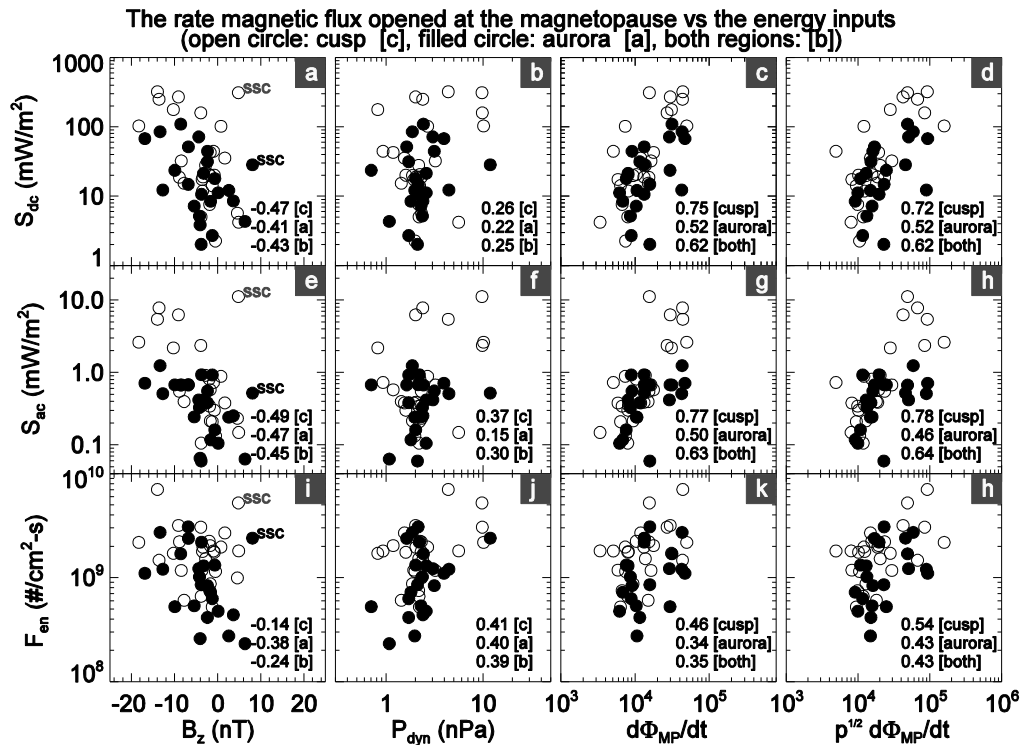
Figure 5. Scatter plots of the energy inputs to the ionosphere, including S_{dc} (top row), S_{ac} (middle row), and f_{en} (bottom row), versus the solar wind-magnetosphere coupling functions, Bz (leftmost column), P_{dyn} (second column from the left), $d\Phi_{MP}/dt$ (third column from the left) and $p^{1/2} d\Phi_{MP}/dt$ (rightmost column), Intensities are averaged over the time period of the dayside cusp outflow (open circle) and the nightside aurora outflow (filled circle). Correlations are computed for the dayside cusp, the nightside aurora, and the both regions, individually.

The energy inputs show a clear negative trend on the IMF Bz, while the slopes are close between the dayside and the nightside source regions, as shown in panels (**a**), (**e**) and (**i**) in Fig. **5**. However, because the average value of Bz is significantly positive during the period of SSC, as shown by the two labeled points when the FAST satellite passed the dayside and the nightside, the computed correlation coefficients are not significant for Bz. It indicates that the energy inputs become enhanced when IMF turns southward and increase with decreasing Bz after the storm SSC. The intensity of the energy inputs does not show a significant correlation with the solar wind dynamic pressure, as shown in panels (**b**), (**f**), and (**j**) in Fig. **5**. In the cusp, S_{dc} and S_{ac} have strong correlations with the first coupling functions, to $d\Phi_{MP}/dt$, with correlation coefficients of 0.75 and 0.77, while the correlation of F_{en} is not as strong, with a correlation coefficient of 0.46. On the nightside, the correlations are weaker, with S_{dc} and S_{ac} having correlation coefficients of 0.52 and 0.50, and F_{en} having a correlation coefficient of 0.34. The correlations with the second coupling function, $p^{1/2} d\Phi_{MP}/dt$ are not significantly different from the correlations with $d\Phi_{MP}/dt$.

4. Summary and conclusions

Nowrouzi et al. (2023) showed that the ionospheric outflow follows a clear pattern during a CME storm, increasing during the initial phase, remaining enhanced during the main phase, and then decreasing during the recovery phase. This study uses one event to track how the IMF and solar wind changes characteristic of a CME-driven storm drive this sequence. The leading edge of a classic CME has a fast forward shock, with increased plasma density and velocity that leads to the sharp

dynamic pressure enhancement. The shock is often followed by a magnetic cloud that has a strong rotating field (**Tsurutani & Gonzlez**, 1997). When the magnetic field is southward, it drives the storm main phase. These characteristic signatures are clearly observed in this storm, as shown in Fig. **1**, with a strong increase in the dynamic pressure and magnetic field magnitude during the initial phase, followed by the strongly southward Bz that coincides with the drop in Dst. The enhanced
375   dynamic pressure and southward Bz both drive energy into the magnetosphere. **Newell** et al. (2007) tested multiple coupling functions to identify the parameters in the solar wind and IMF that most strongly drive the magnetosphere. The two best coupling functions are shown in the last two panels of Fig. **1**. Clearly, the coupling increases strongly during the initial phase of the storm, remains high during the main phase and then decreases during the recovery phase. Figures **3** and **4** show that the outflow observed in this storm is consistent with the statistical picture shown in **Nowrouzi** et al. (2023), with strong
380   outflow during the initial and main phase on both the dayside and nightside, but the strongest outflow on the dayside.

Figure **4** shows how the energy input into the auroral region measured in situ increases during the times when the coupling is strong. The dayside cusp shows a clear response to the changes in the solar wind, with both AC and DC Poynting fluxes as well as soft electron precipitation enhanced during the initial phase and main phase. On the nightside, the overall changes
385   in the energy input are not as clear. The DC Poynting flux shows the clearest increase during the initial phase and main phase, while the AC Poynting flux and the electron precipitation variations with time do not show a strong consistent pattern.

Figure **5** shows the correlation between the energy input into the cusp and nightside auroral regions and the driving parameters from the solar wind and IMF. Consistent with Fig. **4**, the cusp Poynting flux input is well correlated with the
390   coupling function. The dynamic pressure and Bz individually are not so well correlated, but the combination of parameters in the coupling function increases strongly during the storm initial and main phases and drives Poynting flux into the cusp region. The energy from precipitating electrons has a weaker correlation with the driving parameters. Correlations between the nightside energy input and the driving parameters are much weaker.

395   On the dayside, the sequence of events leading to enhanced outflow is clear. The changes in the solar wind due to the CME structure strongly drive the magnetosphere. This enhanced coupling at the magnetopause drives enhanced energy, particularly AC and DC Poynting flux, into the cusp region. This energy input then drives the enhanced outflow. The clear correlations observed on the dayside in this study are possible because during this storm the FAST orbit routinely passes through the localized region of strong energy input on the dayside. That the same clear chain is not observed as strongly on
400   the nightside is likely due to two factors. First, there is some delay between the changes in the solar wind at the magnetopause and the effects on the nightside. The effects of enhanced dynamic pressure are observed almost without delay in the magnetosphere (**Gamarra** et al., 2020), but the response to a southward turning has some delay. The auroral electrojets respond to a southward turning with a delay of less than 5 minutes, and the tail-like deformation of the tail begins in ~10 minutes (**Sauvaud** et al., 1987). But the onset of a substorm driven by the southward turning can take 40-80 minutes
405   (**Sauvaud** et al., 1987; **Samsonov** et al., 2024). These delays will reduce the correlation between the instantaneous solar wind parameters and the energy input. The second factor is that the energy deposited on the nightside is spread over a larger, less continuous region. Thus, it is likely that one spacecraft measuring deposited energy in situ, will sometimes miss the energy input, even if it is significant. That the O^+ outflow does show a clear flux increase on time scales similar to those observed on the dayside indicates that the outflow resulting from energy input may have a longer time duration than the
410   energy input. The outflow would then show a steadier profile, even if the energy input is sporadic. A statistical study of the energy input using a large database of storms, similar to that done by **Nowrouzi** et al. (2023) for outflow, is needed to provide a better statistical estimate of the nightside energy input and response during a storm.

Following the progression of the energy input and the outflow in the auroral zone during a storm with satellite observations
415   is difficult because of the long time scales of the storm compared to the time scales of a low altitude orbit. This storm was fortuitous in that the FAST satellite orbit was in the noon-midnight meridian, and so gave snapshots of the energy input and

ion outflow in both the cusp and the nightside aurora every two hours during the course of the storm. This allowed the time series of the solar wind and IMF, the energy inputs to the dayside and nightside auroral regions, and the dayside and nightside ion outflow to be tracked for the first time during all phases of a single storm. This clearly showed that, while changes in

420   individual solar wind and IMF parameters did not correlate well with the energy inputs to the aurora, the combined changes captured in the **Newell** et al. (2007) coupling functions do correlate with the changes in Poynting flux into the auroral regions. The changes in the Poynting flux drive the strong increases in the outflow observed during the storm.

Acknowledgements

The work at the University of New Hampshire is supported by the NASA Grants 80NSSC19K0073 and 80NSSC19K0363.

425   The first author thanks the support by the National Natural Science Foundation of China (NSFC, Grant No. 41604134) and the support by the Open Project of Center for Applied Mathematics of Jiangsu Province (Nanjing University of Information Science and Technology).

Data availability statement

All observations and measurements made by the FAST spacecraft are available as a level 0 data product through SDT

430   (http://sprg.ssl.berkeley.edu/~sdt/SdtReleases.html). FAST/TEAMS data are available at the NSSDC (**Kistler**, 2023). The OMNI data can be accessed at **Papitashvili** & **King** (2020). The Dst index is available at the provider by **Nose** et al. (2015).

References

Carlson, C. W., McFadden, J. P., Turin, P., Curtis, D. W., & Magoncelli, A. (2001). The Electron and ion Plasma Experiment for Fast. Space Science Reviews, 98, 33-66, doi:10.1023/A:1013139910140.

435   Chaston, C. C., Carlson, C. W., McFadden, J. P., Ergun, R. E., & Strangeway, R. J. (2007). How important are dispersive Alfvén waves for auroral particle acceleration?. Geophysical Research Letters, 34(L07101), doi:10.1029/2006GL029144.

Cohen, I. J., Lessard, M. R., Varney, R. H., Oksavik, K., Zettergren, M., & Lynch, K. A. (2015). Ion upflow dependence on ionospheric density and solar photoionization. Journal of Geophysical Research: Space Physics, 120, 10039–10052, doi:10.1002/2015JA021523.

440   Connor, H. K., Raeder, J., Sibeck, D. G., and Trattner, K. J. (2015). Relation between cusp ion structures and dayside reconnection for four IMF clock angles: OpenGGCM-LTPT results. Journal of Geophysical Research: Space Physics, 120, 4890–4906. doi:10.1002/2015JA021156.

Elphic, R. C., Means, J. D., Snare, R. C., Strangeway, R. J., Kepko, L., & Ergun, R. E. (2001). Magnetic field instruments for the fast auroral snapshot explorer. Space Science Reviews, 98(1-2), 151-168, doi:10.1023/A:1013153623344.

445   Ergun, R. E., Carlson, C. W., Mozer, F. S., Delory, G. T., & Cattell, C. A. (2001). The Fast Satellite Fields Instrument. Space Science Reviews, 98(1), 67-91, doi:10.1023/A:1013131708323.

Gamarra, M. R., Gonzalez, J., Stepanova, M. V., & Antonova, E. E. (2020). Variation of Plasma Pressure at the Auroral Oval Latitudes before, during, and after the Isolated Geomagnetic Substorm on December 22, 2008. Geomagnetism and Aeronomy, 60(4), 452–460, doi:10.1134/s0016793220040131.

450   Ganguli, S. B. (1996). The polar wind. Reviews of Geophysics, 34(3), 311–348, doi:10.1029/96rg00497.

Geiss, J., Balsiger, H., Eberhardt, P., Walker, H. P., Weber, L., Young, D. T., et al. (1978). Dynamics of magnetospheric ion

Composition as observed by the GEOS mass spectrometer. Space Science Reviews, 22(5), 537–566, doi:10.1007/bf00223940.

Harvey, P. R., Curtis, D. W., Heetderks, H. D., Pankow, D., Rauch-Leiba, J. M., Wittenbrock, S. K., et al. (2001). The FAST Spacecraft Instrument Data Processing Unit. Space Science Reviews, 98(1-2), 113–149, doi:10.1023/a:1013135809232.

Hatch, S. M., Chaston, C. C., & LaBelle, J. (2016). Alfvén wave-driven ionospheric mass outflow and electron precipitation during storms. Journal of Geophysical Research: Space Physics, 121(8), 7828–7846, doi:10.1002/2016JA022805.

Hatch, S. M., LaBelle, J., Lotko, W., Chaston, C. C., & Zhang, B. (2017). IMF control of Alfvénic energy transport and deposition at high latitudes. Journal of Geophysical Research: Space Physics, 122, 12, 12189-12211, doi:10.1002/2017JA024175.

Hatch, S. M., Moretto, T., Lynch, K. A., Laundal, K. M., Gjerloev, J. W., & Lund, E. J. (2020). The relationship between cusp region ion outflows and east-west magnetic field fluctuations at 4,000-km altitude. Journal of Geophysical Research: Space Physics, 125, e2019JA027454, doi:10.1029/2019JA027454.

Hull, A. J., Chaston, C. C., & Damiano, P. A. (2023). Multipoint Cluster Observations of Kinetic Alfvén Waves, Electron Energization, and O^+ Ion Outflow Response in the Mid-Altitude Cusp Associated With Solar Wind Pressure and/or IMF BZ Variations. Journal of Geophysical Research: Space Physics, 128(11), e2023JA031982, doi:10.1029/2023ja031982.

Kistler, L. M. (2023). FAST/TEAMS energy-pitch angle distributions [Dataset]. NASA Space Physics Data Facility. Retrieved from https://spdf.gsfc.nasa.gov/pub/data/fast/teams/l2/pa/.

Kistler, L. M., Mouikis, C. G., & Genestre, K. J. (2013). In-flight calibration of the Cluster/CODIF sensor. Geoscientific Instrumentation, Methods and Data Systems, 2, 225–235, doi:10.5194/gi-2-225-2013.

Kitamura, N., Seki, K., Keika, K., Nishimura, Y., Hori, T., Hirahara, M., et al. (2021). On the relationship between energy input to the ionosphere and the ion outflow flux under different solar zenith angles. Earth Planets Space, 73, 202, doi:10.1186/s40623-021-01532-y.

Klumpar, D. M., Möbius, E., Kistler, L. M., Popecki, M., Hertzberg, E., Crocker, K., et al. (2001). The Time-of-Flight Energy, Angle, Mass Spectrograph (TEAMS) Experiment for FAST. Space Science Reviews, 98, 197–219, doi:10.1007/978-94-010-0332-2_8.

Lund, E. J., Möbius, E., Klumpar, D. M., Kistler, L. M., Popecki, M. A., Klecker, B., et al. (1999). Direct comparison of transverse ion acceleration mechanisms in the auroral region at solar minimum. Journal of Geophysical Research, 104(A10), 22801–22805, doi:10.1029/1999ja900265.

Lund, E. J., Möbius, E., Carlson, C. W., Ergun, R. E., Kistler, L. M., Klecker, B., et al. (2000). Transverse ion acceleration mechanisms in the aurora at solar minimum: occurrence distributions. Journal of Atmospheric and Solar-Terrestrial Physics, 62(6), 467–475, doi:10.1016/s1364-6826(00)00013-4.

McFadden, J. P., Carlson, C. W., Ergun, R. E., Mozer, F. S., Temerin, M., Peria, W., et al. (1998). Spatial structure and gradients of ion beams observed by FAST. Geophysical Research Letters, 25(12), 2021–2024, doi:10.1029/98gl00648.

Möbius, E., Tang, L., Kistler, L. M., Popecki, M., Lund, E. J., Klumpar, D., et al. (1998). Species dependent energies in upward directed ion beams over auroral arcs as observed with FAST TEAMS. Geophysical Research Letters, 25(12), 2029–2032, doi:10.1029/98gl00381.

Newell, P. T., Sotirelis, T., Liou, K., Meng, C.-I., & Rich, F. J. (2007). A nearly universal solar wind-magnetosphere coupling function inferred from 10 magnetospheric state variables. Journal of Geophysical Research, 112, A01206, doi:10.1029/2006JA012015.

Nosé, M., Taguchi, S., Christon, S. P., Collier, M. R., Moore, T. E., & Carlson, C. W., et al. (2009). Response of ions of

ionospheric origin to storm time substorms: Coordinated observations over the ionosphere and in the plasma sheet. Journal of Geophysical Research, 114(A5), A05207, doi:10.1029/2009ja014048.

Nose, M., Iyemori, T., Sugiura, M., & Kamei, T. (2015). Geomagnetic Dst index [Dataset]. World Data Center for Geomagnetism. doi:10.17593/14515-74000.

Nowrouzi, N., Kistler, L. M., Zhao, K., Lund, E. J., Mouikis, C., Payne, G., & Klecker, B. (2023). The variation of ionospheric O^+ and H^+ outflow on storm timescales. Journal of Geophysical Research: Space Physics, 128, e2023JA031786, doi:10.1029/2023JA031786.

Nowrouzi, N. (2022). Ionospheric O^+ and H^+ Outflow During Geomagnetic Storms. ProQuest Dissertations Publishing.

Papitashvili, N. E., & King, J. H. (2020). OMNI 1-min data set. [Dataset]. NASA Space Physics Data Facility. doi:10.48322/45bb-8792.

Peterson, W. K., Tung, Y.-K., Carlson, C. W., Clemmons, J. H., Collin, H. L., Ergun, R. E., et al. (1998). Simultaneous observations of solar wind plasma entry from FAST and POLAR. Geophysical Research Letters, 25(12), 2081–2084, doi:10.1029/98gl00668.

Peterson, W. K., Collin, H. L., Lennartsson, O. W., & Yau, A. W. (2006). Quiet time solar illumination effects on the fluxes and characteristic energies of ionospheric outflow. Journal of Geophysical Research, 111(A11), A11S05, doi:10.1029/2005ja011596.

Pfaff, R., Carlson, C., Watzin, J., Everett, D., & Gruner, T. (2001). An Overview of the Fast Auroral Snapshot (FAST) Satellite. In: Pfaff R.F. (eds) The FAST Mission. Springer, Dordrecht, doi:10.1007/978-94-010-0332-2_1.

Russell, C. T., Wang, Y. L., Raeder, J., Tokar, R. L., Smith, C. W., Ogilvie, K. W., et al. (2000). The interplanetary shock of September 24, 1998: Arrival at Earth. Journal of Geophysical Research, 105(A11), 25143–25154, doi:10.1029/2000ja900070.

Samsonov, A., Milan, S., Buzulukova, N., Sibeck, D., Forsyth, C., Branduardi-Raymont, G., & Dai, L. (2024). Time Sequence of Magnetospheric Responses to a Southward IMF Turning. Journal of Geophysical Research: Space Physics, 129(7), doi:10.1029/2023ja032378.

Sauvaud, J. A., Treilhou, J. P., Saint-Marc, A., Dandouras, J., Rème, H., Korth, A., et al. (1987). Large scale response of the magnetosphere to a southward turning of the interplanetary magnetic field. Journal of Geophysical Research: Space Physics, 92(A3), 2365–2376, doi:10.1029/ja092ia03p02365.

Shelley, E. G., Johnson, R. G., & Sharp, R. D. (1972). Satellite observations of energetic heavy ions during a geomagnetic storm. Journal of Geophysical Research, 77(31), 6104–6110, doi:10.1029/JA077i031p06104.

Strangeway, R. J., Ergun, R. E., Su, Y.-J., Carlson, C. W., & Elphic, R. C. (2005). Factors controlling ionospheric outflows as observed at intermediate altitude. Journal of Geophysical Research, 110, A03221, doi:10.1029/2004JA010829.

Tsurutani, B. T., & Gonzalez, W. D. (1997). The Interplanetary causes of magnetic storms: A review. Magnetic Storms, 98, 77–89, doi:10.1029/gm098p0077.

Wilson, G. R., Ober, D. M., Germany, G. A., & Lund, E. J. (2001). The relationship between suprathermal heavy ion outflow and auroral electron energy deposition: Polar/Ultraviolet Imager and Fast Auroral Snapshot/Time-of-Flight Energy Angle Mass Spectrometer observations. Journal of Geophysical Research, 106(A9), 18981–18993, doi:10.1029/2000ja000434.

Yao, Y., Seki, K., Miyoshi, Y., McFadden, J. P., Lund, E. J., & Carlson, C. W. (2008). Effect of solar wind variation on low-energy O^+ populations in the magnetosphere during geomagnetic storms: FAST observations. Journal of Geophysical Research, 113(A4), A04220, doi:10.1029/2007ja012681.

Zhao, K., Kistler, L. M., Lund, E. J., Nowrouzi, N., Kitamura, N., & Strangeway, R. J. (2020). Factors controlling O^+ and

H$^+$ outflow in the cusp during a geomagnetic storm: FAST/TEAMS observations. Geophysical Research Letters, 47(11), e2020GL086975, doi:10.1029/2020GL086975.

Zhao, K., Kistler, L. M., Lund, E. J., Nowrouzi, N., Kitamura, N., & Strangeway, R. J. (2022). Nightside Auroral H$^+$ and O$^+$ Outflows Versus Energy Inputs During a Geomagnetic Storm. Journal of Geophysical Research: Space Physics, 127, e2022JA030923, doi:10.1029/2022JA030923.

Zheng, Y., Moore, T. E., Mozer, F. S., Russell, C. T., & Strangeway, R. J. (2005). Polar study of ionospheric ion outflow versus energy input. Journal of Geophysical Research, 110, A07210, doi:10.1029/2004JA010995.

535